# Quantitative analysis of cyclic aging of lithium-ion batteries using synchrotron tomography and electrochemical impedance spectroscopy

Alexander Ridder[a,*], Benedikt Prifling[b,*,**], André Hilger[c], Markus Osenberg[d], Matthias Weber[b], Ingo Manke[c], Kai Peter Birke[a], Volker Schmidt[b]

[a] *Electrical Energy Storage Systems, Institute for Photovoltaics, University of Stuttgart, 70569 Stuttgart, Germany*
[b] *Institute of Stochastics, Ulm University, 89069 Ulm, Germany*
[c] *Institute of Applied Materials, Helmholtz Center for Materials and Energy, 14109 Berlin, Germany*
[d] *Department of Materials Science and Technology, Technische Universität Berlin, 10623 Berlin, Germany*

**Abstract**

The highly complex aging mechanisms of lithium-ion batteries are still not sufficiently well understood. In the present paper, we characterize cyclically aged cells by means of a statistical 3D microstructure analysis and electrochemical properties. More precisely, synchrotron tomography is used to capture the morphology of lithium-ion battery cathodes with a state of health of 100%, 90%, 80%, 60% and 40%, cyclically aged with two different C-rates (0.5C and 1C). The three phases, namely active material, pores and the phase carbon-binder domain, have been reconstructed from 3D grayscale images by a $k$-means clustering approach. Moreover, individual active particles are segmented by combining the concept of morphological reconstruction with the watershed algorithm. The processed image data allows to quantitatively characterize the 3D microstructure by phase-based and particle-based characteristics, where a special focus is put on local heterogeneity, which will be described by locally computed descriptors. In addition, electrochemical data and electrochemical impedance spectroscopy are used to characterize the cyclically aged cells. Furthermore, we correlate these results with the detected structural changes. To the best of our knowledge, this is the most extensive data set of cyclically aged lithium-ion cells including electrochemical data as well as 3D structures.

*Keywords:* cathode, lithium-ion battery, cyclic aging, microstructure, electrochemical impedance spectroscopy, synchrotron tomography

## 1. Introduction

Lithium-ion batteries are one of the key technologies of recent and future years due to their high energy density as well as a decent power density, which leads to a variety of applications ranging from portable devices to electric vehicles [1, 2, 3, 4, 5]. To further reduce costs and the environmental impact of lithium-ion batteries, one of the main goals in state-of-the-art battery research is to increase their lifetime [6, 7, 8]. Therefore, a deeper understanding of the complex aging mechanisms, which are still not fully understood, is key with regard to the development of electrodes with optimized electrochemical properties [9, 10]. To analyse the aging mechanisms with electrochemical methods electrochemical impedance spectroscopy (EIS) is used frequently. The gained data are often fitted with an equivalent circuit model (ECM) based on simple electronic components as resistors and capacitors [11]. ZARC

*Equally contributing authors that share first authorship.
**Corresponding author. Email: benedikt.prifling@uni-ulm.de Phone: +49 731 50 23555

elements can be used to fit the EIS data instead of RC elements in ECMs. Though they can describe the data better than the same mount of RC elements yet their physicochemical interpretation is not fully defined at this point [12].

Since it is well known that the 3D microstructure of battery electrodes has a strong impact on the resulting effective properties [13, 14, 15, 16], the microstructural changes caused by cyclic aging are of particular interest. For this purpose, imaging techniques such as electron spectroscopy, X-ray diffraction or X-ray photoelectron spectroscopy are used [17, 18, 19, 20]. Since lithium-nickel-cobalt-manganese oxides (NCMs) are still the basis for most industrially manufactured cathodes [21], the focus of the present paper is to quantitatively investigate the cyclic aging of NCM-based cells by means of EIS and synchrotron tomography to gain a deeper understanding of the aging mechanisms, both, from a structural as well as an electrochemical point of view.

In the present paper, we characterize cyclically aged cells by means of a statistical 3D microstructure analysis and electrochemical properties. More precisely, synchrotron tomography is used to capture the morphology of lithium-ion battery cathodes with a state of health of 100%, 90%, 80%, 60% and 40%, cyclically aged with two different C-rates (0.5C and 1C). The three phases, namely active material, pores and the phase consisting of binder and conductive additives, have been reconstructed from 3D grayscale images by a $k$-means clustering approach. Moreover, individual active particles are segmented by combining the concept of morphological reconstruction with the watershed algorithm. The processed image data allows to quantitatively characterize the 3D microstructure by phase-based as well as particle-based characteristics, where a special focus is put on local heterogeneity, which will be described by locally computed descriptors. In addition to the structural point of view, electrochemical data and EIS are used to characterize the cyclically aged cells. Finally, the results of the statistical microstructure analysis are correlated with the parameters of the ECM, which is fitted to data obtained by electrochemical impedance spectroscopy.

The rest of this paper is organized as follows. In Section 2, the cyclic aging of the cells as well as the imaging of the NCM-based cathodes is described. Next, we describe the processing of the 3D image data consisting of image preprocessing, a three-phase reconstruction and a particle-based segmentation of the active particles. In Section 4, a variety of phase-based as well as particle-based characteristics are described, which will be used to quantitatively investigate the influence of cyclic aging on the morphology of the cathodes. In addition, EIS data are analysed with an ECM to quantify the influence of cyclic aging on the electrochemical behaviour of the cells, see Section 5. Finally, the paper is concluded with a summary of the results in Section 6.

## 2. Experimental

In this section, we describe the material composition, the cyclic aging procedure and the imaging process in detail.

### *2.1. Materials*

In the present paper, we consider nine one-layered pouch cells with about 40 mA h at C/10, manufactured by VARTA Microbattery GmbH. The composition of the electrodes manufactured by a representative research recipe and the densities of the used materials are listed in Table 1. Additionally, an areal weight of 180 g/m$^2$ and an electrode thickness of 60 µm for the cathode allow us to compute the volume fraction of the cathode materials, which will be used for image segmentation in Section 3.

| component | portion [wt%] | density [g/cm$^3$] |
|---|---|---|
| NCM622 | 94-95 | 4.76 |
| binder | ca. 1 | 1 |
| conductive additive | 3-4 | 2 |
| graphite | 96-97 | 2 |
| binder | ca. 2 | 1 |
| conductive additive | ca. 1 | 2 |

Table 1: Material composition of cathodes and anodes and density of materials.

### *2.2. Cyclic aging*

Cyclic aging and EIS measurements were done using a Basytec CTS connected via a multiplexer with a Gamry Reference 3000. The pristine cells provided by VARTA Microbattery GmbH were characterized at different C-rates to determine their performance and discharge capacity. To investigate the influence of cyclic aging on the electrode morphology as well as their electrochemical behavior, eight cells were aged to a state of health (SOH) of 90%, 80%, 60% and 40%, respectively. More precisely, for each SOH there are two cells that differ with regard to their C-rate, where we considered the C-rates of 0.5C and 1C. To compute the corresponding currents for these two C-rates, we determine the individual capacity of each cell at 1/10C using the nominal capacity. The current for the aging procedure is then computed from the individual capacity. The capacity of each cell at cyclic aging speed is used to determine the SOH in comparison to the discharge capacity in the individual cycle. All cells were cycled with CC-CV full cycles. One cell remained in its original state at 100% SOH and was used as reference.

### *2.3. Electrochemical impedance spectroscopy*

All cells were characterized by EIS measurements in galvanostatic mode every 50th cycle with four hours relaxation time beforehand at 0% SOC. For this purpose, a frequency range from 10 kHz to 10 mHz with ten points per decade and an AC current of 4 mA (0.1C of nominal capacity) have been used. To account for changing connection resistances, measurements with an internal resistance at least three times higher than in the first measurement for the same cell are corrected in their real part of the impedance. This is done by computing the mean change in internal resistance up to the (to be corrected) measurement and using this value times the number of impedance measurements until this point as new internal resistance. The other values for the real part of the impedance of the measurement are adjusted by the same factor. Note, that Matlab 2021b is used to analyze the electrochemical data including the EIS measurements and the ECM.

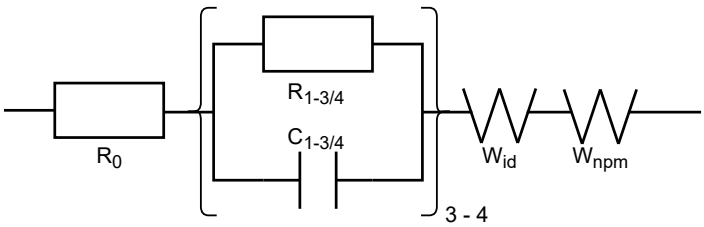


Figure 1: Used ECM to analyze the EIS data.

The results were fitted with an equivalent circuit model (ECM) in the form R-RC-RC-RC-W-W as presented in Figure 1. This ECM covers all processes in the cell on cathode and anode side. The first resistor (R0) resembles the ohmic resistance of connections and the internal resistance of the cell. The RC-circuits are simulating the following processes in the cell, which are listed in increasing order of their characteristic time scale: electron transfer current collector-electrodes as well as particle-particle resistance, ionic passage graphite-electrolyte, NCM-electrolyte and electrolyte-separator. The Warburg impedance consists of two parts: diffusion in the electrolyte and diffusion inside the active material of the electrodes, represented by a Warburg impedance with an ideal reservoir $W_{id}$ as well as a non-permeable membrane $W_{npm}$, respectively. As we only analyze 3D image data of the cathodes, the RC-element that covers the electrode-electrolyte transfer is split to analyze cathode and anode separately. To prevent inconsistent fitting, several constraints regarding the fitting are used. For example, the capacitance for the capacitors was kept in range to each other, avoiding the case of one dominating factor and a few very minimal capacitors. To differentiate between cathode and anode processes, the second RC-parallel circuit is divided into two parts at different scales.Considering the approximated surface area, computed by surface areas per gram from [22] and [23], electrode loading, and typical exchange current densities it is likely that the cathode is responsible for about 90% of the resistance caused by the electrolyte-electrode transfer. Hence, the graphite RC circuit is restricted to 5-15% of the overall resistance, whereas the RC circuit corresponding to NCM electrode is constrained to 85-95% of the former second RC-element.

### *2.4. Sample preparation and imaging procedure*

After reaching their destined SOH the cells were discharged to 2.5 V and disassembled under argon atmosphere ($< 0.5$ ppm $H_2O$ and $< 0.5$ ppm $O_2$). The electrodes were washed in dimethyl carbonate for 30 seconds and cut into smaller pieces in preparation for the synchrotron tomography experiments.

The tomography measurements of the cathode samples have been conducted at two separate synchrotron facilities. The samples 100%, 90% 0.5C, 90% 1C, 80% 1C and 40% 1C have been measured at the P05 beamline (Petra III, DESY, Germany) [24, 25], whereas the samples 80% 0.5C, 60% 0.5C, 40% 0.5C, 60% 1C have been measured at the BAMline (BESSY II, HZB, Germany) [26]. The working principle of both beamlines is similar, in both cases a monochromatic nearly parallel X-ray beam is guided on the rotating sample without the use of X-ray focusing optics. Behind the sample the transmitting beam is detected with a setup consisting of a $CdWO_4$ scintillator for X-ray to light transformation, an optical microscope and a CMOS camera.

In case of the P05 beamline, the pristine sample has been measured with an energy of 28 keV, while the remaining P05 samples have been measured with 25 keV to assure an optimal image contrast. For energy selection a double crystal monochromator was used. All samples have been measured as close as possible to the scintillator screen to reduce phase contrast. During the tomography each sample was constantly rotated while 2401 images have been capture using a KIT CMOS camera (5120 × 3840 pixel) with an exposure time of 130 ms. Combined with the 10 times optics this resulted in a voxel size of 0.64 µm. For the reconstruction the normalized data was denoised using a total variation minimization filter [27] and then reconstructed using the gridrec routine based on the filtered back projection [28].

In case of the BAMline, the samples 80% 0.5C, 60% 0.5C, 40% 0.5C and 60% 1C have been measured with 25 keV. In contrast to P05, the energy selection at BAMline was done by using a double multi layer monochromator, resulting in a slightly broader energy spectrum around the mentioned target energy. The samples have been measured as close to the detector as possible. At BAMline, the samples have

been rotated stepwise, so for each image the rotation was halted. Every hundredth rotation step the sample was removed from the field of view for flatfield capture. In addition, the center of rotation was randomly altered after each flatfield sequence. During the post processing the known shift of the center of rotation was removed resulting in a slightly smaller field of view but also removing all ring artifacts. In total, 2200 projections were measured, where a PCO4000 camera (4008 × 2672 pixel) was used for image acquisition, resulting in a voxel size of 0.44 µm. The reconstruction was done in the same way as in the case of the P05 data. Note that linear interpolation is used to scale the P05 samples (voxel size 0.64 µm) to the voxel size of 0.44 µm [29].

## 3. Image processing

This section describes the image processing methods that are applied to the 3D image data obtained by synchrotron tomography. This includes image preprocessing, the three-phase reconstruction of the preprocessed grayscale image data as well as the segmentation of individual active particles.

### *3.1. Image preprocessing*

At first, a non-local means filter with a local neighborhood size of one and a search volume size of 11 voxels is applied, which significantly reduces the noise while preserving edges [30, 31]. Afterwards, the 3D image data is rotated such that the first slices correspond to the current collector, i.e., the $z$-direction now corresponds to the main direction of ionic and electric transport. The rolling ball method, which is based on a morphological closing, is used to define a mask of the electrode (excluding the current collector) [32]. By doing so, one is not restricted to a cuboid that is fully contained within the sample and is able to take the complete volume of the electrode into account.

### *3.2. Phase-based segmentation*

Note that the voxel size of 0.44 µm is larger than the size of binder as well as conductive additives. Thus, we will assign a nanoporosity of 50% to the carbon-binder domain (CBD), where similar values of 47% and 58% are reported in the literature [33, 34]. In order to trinarize the preprocessed grayscale images, i.e., segmenting them into the three phases, active material, pores and the carbon binder domain (called CBD in the following), we use a modified $k$-means clustering algorithm similar to [20]. However, the present approach allows us to match the known target volume fraction of the pristine sample by tuning certain parameters accordingly. Applying the modified $k$-means cluster algorithm with the parameters obtained from the pristine cathode to the cyclically aged samples allows us to reconstruct the three phases with one and the same approach. More precisely, the newly introduced parameters consist of phase weights as well as feature weights. In order to formally define them, we introduce the following notation. Let $v_1, ..., v_n$ denote the voxels inside the mask of the electrode, where for each voxel $v_i$ a so-called feature vector $f_i = (f_i^{(1)}, ..., f_i^{(27)}) \in \mathbb{R}^{27}$ is considered, which consists of the sorted grayvalues within the $3 \times 3 \times 3$ neighborhood of $v_i$. The $k$-means clustering algorithm partitions $v_1, ..., v_n$ into $k = 3$ clusters $C_1, C_2, C_3$, which correspond to the three phases, namely active material, pores and CBD. More precisely, it holds

$$C_j = \{v_i \ : \ j = \underset{\ell=1,2,3}{\operatorname{argmin}} w_\ell \cdot \sum_{m=1}^{27} x_m \cdot (f_i^{(m)} - \mu_\ell^{(m)})^2\} \qquad \text{for } j \in \{1,2,3\}, \tag{1}$$

where $w_1, w_2, w_3 > 0$ denote the phase weights, $x_1, ..., x_{27} > 0$ the feature weights and $\mu_\ell = (\mu_\ell^{(1)}, ..., \mu_\ell^{(27)}) \in \mathbb{R}^{27}$ the feature vector of the centroid of the $\ell$-th cluster, respectively. In the classical $k$-means

approach, the phase weights as well as the feature weights are all equal to one. To reduce the dimension of the optimization problem, we set $w_1 = 1$ and $x_1 = 1$ as reference. In addition, we assign equal feature weights to voxels within the $3 \times 3 \times 3$ neighborhood, which have the same (discretized) Euclidean distance to the currently considered voxel $v_i$. This results in the following five parameters, which are subject to the optimization: The phase weights $w_2$ and $w_3$ as well as the feature weights $x_2$ (used for the 6 voxels with distance one), $x_8$ (used for the 12 voxels with distance $\sqrt{2}$) and $x_{20}$ (used for the 8 voxels with distance $\sqrt{3}$). Powell's BOBYQA algorithm is then used to minimize the sum of squared differences between the experimentally determined volume fractions and the volume fractions obtained by the modified $k$-means cluster algorithm [35].

### *3.3. Particle-based segmentation*

Based on the three-phase reconstruction described above, individual particles will be distinguished from each other using the marker-based watershed algorithm [36, 37, 38]. This frequently used technique typically leads to oversegmentation, which can be mitigated by means of approaches such as the concept of extended regional minima [39] or a post-processing step based on dilation [40]. Even though the combination of these techniques is able to successfully segment active particles in cathodes of lithium-ion batteries [20, 41], there are two parameters, which have to be tuned manually. To reduce the effort of manual parameter tuning, the segmentation of active particles in the present paper is carried out via the straightforward adaption of the 2D morphological reconstruction approach presented in [42] to 3D. More precisely, the Euclidean distance transform $D$ from the active material to its complement is computed [29, 43, 44]. Afterwards, a morphological reconstruction using $D$ as mask and $(1-\alpha)D$ as marker with $\alpha \in (0,1)$ is carried out [45, 46, 47], leading to the reconstructed distance transform $R$ [48]. The marker image is now given by the local maxima of $R$, whereas the watershed transformation is performed on $-R$. The reconstruction step merges two local maxima $d_1 \geq d_2 > 0$ of $D$ if and only if $\frac{w}{d_2}$ is larger or equal than $1-\alpha$, where $w$ denotes the value of $D$ at the watershed line separating $d_1$ and $d_2$. For detailed visualizations of the morphological reconstruction process, we refer to [42]. Thus, the particle-based segmentation only requires manual tuning of the parameter $\alpha$. It turns out that $\alpha = 0.2$ is a reasonable choice, which allows us to successfully segment the NCM particles of all samples, see Figure 2. Note that using the algorithm proposed in [48] allows to efficiently compute morphological reconstructions such that the present method is also advantageous from a computational point of view.

## 4. Microstructure descriptors

This section covers the definition of several phase-based and particle-based image characteristics. A particular focus is put on quantifying the spatial heterogeneity by means of locally computed descriptors of 3D microstructure.

### *4.1. Volume fraction*

Obviously, the volume fraction $\varepsilon \in [0,1]$ of a certain phase is a fundamental characteristic of great importance, which can be easily estimated from voxelized image data by the point count method [49]. Note that the volume fractions of the three phases have been in used in Section 3.2 to obtain suitable segmentation parameters by matching the experimentally determined volume fractions of the pristine cathode.

### *4.2. Specific surface area*

The specific surface area $S \geq 0$ (SSA) of a predefined phase is given by the ratio of its surface area and the volume of the observation window. The surface area is estimated by weighted local $2 \times 2 \times 2$ voxel configurations, where the weights proposed in [50] are used.

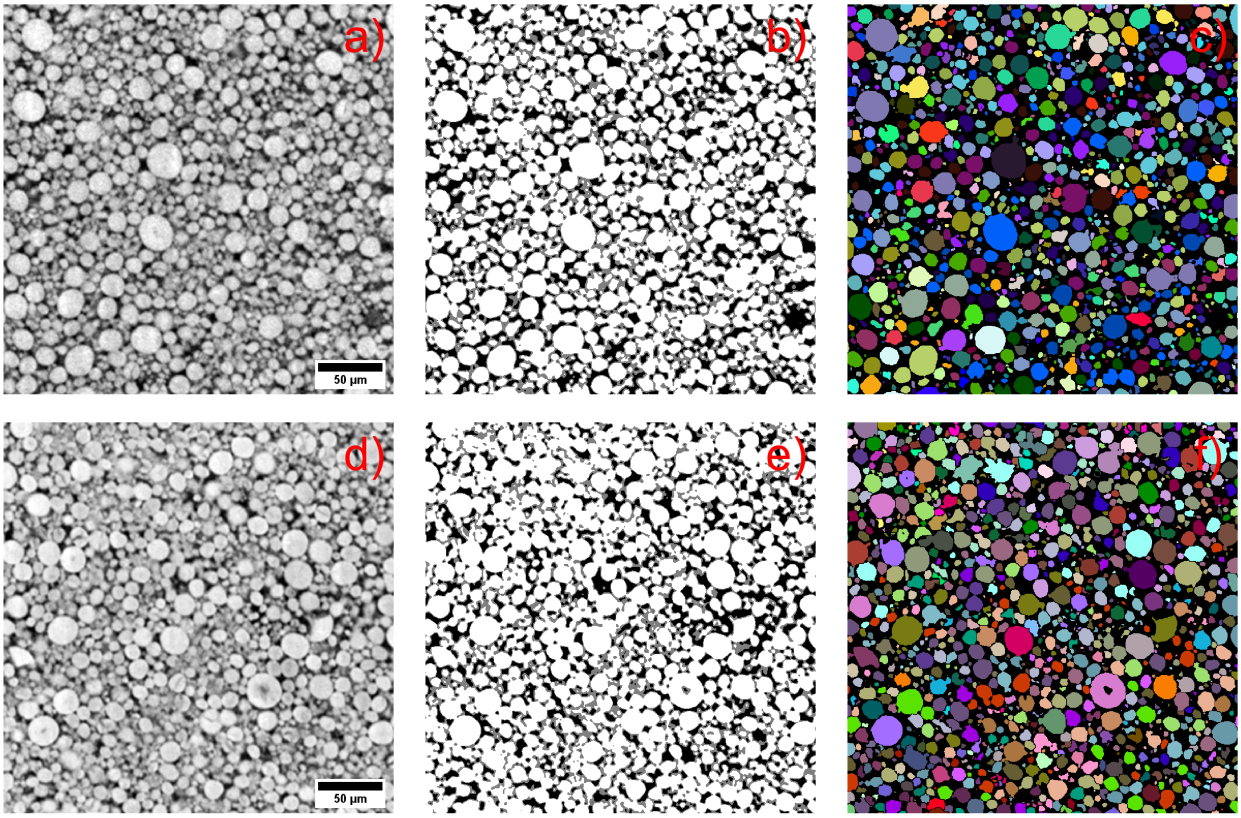


Figure 2: Two-dimensional in-plane cutouts (300 µm × 300 µm) of the pristine cathode (a-c) and a cyclically aged cathode (SOH 80 %, 1C, (d-f)), where the left column (a,d) contains the grayscale images. The center column (b,e) shows the corresponding trinarizations, where active material, CBD and pores are depicted in white, gray and black, respectively. The segmentation of active particles is shown in the right column (c,f), where different colors are used to label the individual active particles.

### *4.3. Geodesic tortuosity*

A further phase-based microstructure descriptor is the geodesic tortuosity of a certain phase, which is a purely geometric characteristic based on shortest paths. At this point, note that different concepts of tortuosity exist in the literature, which is a common source of confusion [51, 52, 53]. When considering geodesic tortuosity, for each point within the starting region, the shortest path to the target region is computed, where the shortest paths have to be completely contained in a predefined phase. Geodesic tortuosity is now defined as the length of those shortest paths divided by the Euclidean distance between the respective start and end points, resulting in a distribution of tortuosity values greater or equal to one. Mean geodesic tortuosity $\tau_{\text{geo}} \geq 1$ is then simply obtained by averaging over all tortuosity values. In general, this characteristic is closely related to effective transport properties, see [54, 55, 56]. In the present paper, the shortest paths are computed from the current collector side to the separator side (i.e. in $z$-direction) since this is the main direction of electric and ionic transport. For this purpose, the well-known Dijkstra algorithm is used [57]. Note that for each pair $(x, y)$ of $x-$ and $y-$coordinates, we add the voxel with the lowest $z$-coordinate that belongs to the mask of the electrode to the starting region if this voxel belongs to the phase on which transport takes place. Analogously, the target region is based on the voxels with the highest $z$-coordinate that are located inside the mask and are part of the transport phase. A more formal definition of geodesic tortuosity within the framework of random closed sets can be found in [58].

### 4.4. Continuous phase size distribution

The continuous phase size distribution $\mathsf{CPSD} : [0,\infty) \to [0,1]$ is defined in terms of morphological openings [46, 45], which is the reason why this phase-based characteristic is sometimes called opening size distribution [59, 46]. In particular, for each fixed radius $r \geq 0$, a morphological opening of the considered phase is carried out using a sphere with radius $r$ as structuring element. The value $\mathsf{CPSD}(r)$ is now given by the volume of the phase of interest after opening. This corresponds to the maximum volume that can be covered by spheres with radius $r$, which have to be completely contained inside the considered phase.

### 4.5. Particle size distribution

One of the most fundamental particle-based characteristic is the distribution of particle sizes, which will be quantified by volume-equivalent radii.

### 4.6. Sphericity

In order to characterize the roundness of active particles, we consider the sphericity, which is defined by $\psi = \frac{\sqrt[3]{\pi}}{A}(6V)^{\frac{2}{3}} \in [0,1]$, where $A$ and $V$ denote the surface area and the volume of an active particle, respectively. This quantity, originally introduced in [60], is equal to one if and only if the particle is a sphere. The lower the sphericity, the larger the deviation of the particle shape from a perfect sphere.

### 4.7. Connectivity

The connectivity of the active particle system is quantified by the distribution of coordination numbers. The coordination number of a single particle is defined as the number of touching particles, where the $3 \times 3 \times 3$ neighborhood is used to decide whether two discretized active particles touch each other.

### 4.8. Local characteristics

It is well known that, besides the overall morphology of battery electrodes, local heterogeneities also strongly affect the electrochemical performance [61, 62, 63]. In particular, degradation mechanisms [64], lithium-plating [65], electronic impedance [66] and effective tortuosity [67, 68] are potentially subject to large variations on a local scale. Thus, we partition the observation window into equally sized cutouts with 50 voxels in $x$- and $y$-direction, whereas the whole sample thickness is used in $z$-direction (through-plane direction). By computing a given descriptor of 3D microstructure for each small cutout, one obtains the local distribution of this characteristic, which allows us to quantify the heterogeneity of the electrode.

## 5. Results

In this section we discuss the results obtained by statistical image analysis and electrochemical measurements to quantify the effects of cyclic aging.

### 5.1. Statistical microstructure analysis

First, using the microstructure descriptors considered in Section 4, we discuss the structural changes of cathodes caused by the different cycling conditions. The top row of Figure 3 shows the volume fractions of active material (NCM), CBD as well as pore space of the nine samples with a state of health (SOH) of 100%, 90%, 80%, 60% and 40%, respectively. Generally, the volume fraction of NCM is slightly increasing during aging by 1.7% to 4.1%. Note that for a SOH of 80 % and 40%, the charging rate of 1C leads to a slightly lower volume fraction of NCM compared to 0.5C, whereas both C-rates behave similarly in

case of a state-of-health of 90 % and 60%. In contrast to the active material, the volume fraction of CBD and the porosity decrease during cyclic aging. Moreover, there seems to be no unambiguous behavior for the different cycling rates, especially for the pore phase. With regard to active material and CBD, we observe a slightly stronger effect for the 0.5C samples. Furthermore, the probability density of the local volume fraction of NCM is clearly shifted to the right for decreasing SOH-values, see the middle row of Figure 3. In addition, the C-rate has a considerable impact on the location and shape of this density when considering SOH values less or equal than 80%. This effect is similar when considering the CBD instead, where cyclic aging generally leads to lower local CBD volume fractions resulting in a shift of the probability density to the left. With regard to the distribution of local porosity, the increased fraction of regions with a quite small porosity caused by cyclic aging is of particular interest, since this might cause bottleneck effects hindering ionic transport.

In contrast to the relatively small changes of global volume fractions and somewhat larger changes of (horizontally) local volume fractions discussed above, there are more pronounced gradients in through-plane direction, see the bottom row of Figure 3. Note that even the pristine cathode sample exhibits a slight CBD gradient. This is likely caused by binder migration [69, 70, 71, 72], which in turn causes the active material gradient. The cyclically aged samples show stronger variations in through-plane direction with regard to the volume fractions of all three phases compared to the pristine sample. Furthermore, for a state of health of 90 %, the differences between 0.5C and 1C are quite small, whereas for lower SOH-values, the C-rate has a significant impact. In general, the volume fraction of the pores strongly decreases when considering the region of the electrode that is at most 10 µm away from the current collector. With regard to the remaining part of the electrode, this quantity varies only about 5%.

The top row of Figure 4 shows the specific surface area (SSA) of each phase. It can be seen that cyclic aging leads to a larger surface area of active material, which might be due to particle cracking. An increase in specific surface area is also observed with regard to the CBD, despite the slight decrease of the CBD volume fraction. However, the specific surface area of the pore space is not significantly affected by cyclic aging, except for both 60% SOH cells, which show an increase (1C) or decrease (0.5C) compared to pristine sample. Furthermore, the middle row of Figure 4 shows that cyclic aging leads to an increased number of regions with a comparatively large specific surface area of the active material. On the other hand, with regard to the CBD as well as the pore space, there is no clear shift of the distribution of local specific surface area. Note that the most pronounced changes with regard to these two phases is observed for the samples with a state of health of 60%.

Note that also the specific surface area strongly depends on the distance to the current collector, see the bottom row of Figure 4. More precisely, most cells show an approximately linear increase of the specific surface area of the active material along the course from the current collector to the separator. With regard to the CBD, the specific surface area is highly correlated to the corresponding volume fraction curve in shown in Figure 3h). When considering the specific surface area of the pore space for distances larger than 10 µm, the variations along the transport direction are strongly pronounced in contrast to the more homogeneous behavior of the distance-dependent volume fraction.

Figure 5 shows the mean geodesic tortuosity of the three phases. In general, a tendency towards larger values of the mean geodesic tortuosity for decreasing SOH values can be observed, where the microstructural changes with regard to this quantity are much less pronounced compared to the previously considered characteristics.

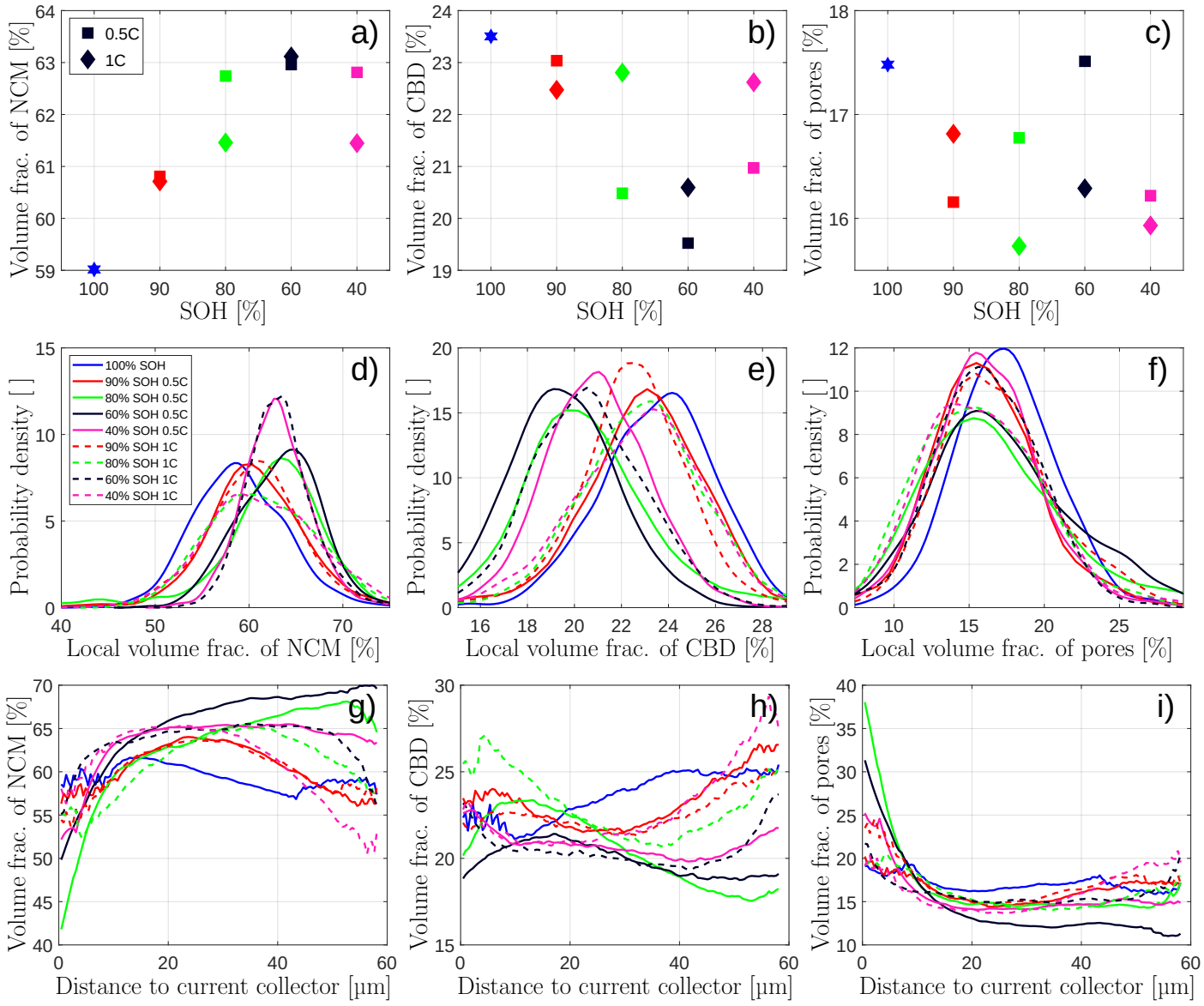


Figure 3: Top row: Volume fraction of active material (a), CBD (b) and pore space (c). Center row: Probability density of local volume fraction of active material (d), CBD (e) and pore space (f). Bottom row: Volume fraction of active material (g), CBD (h) and pore space (i) as a function of the distance to the current collector.

Next, we consider the continuous phase size distribution of CBD and pore space, see Figure 6. It can be observed that the continuous phase size distribution of these two phases is not influenced by cyclic aging. In addition, the size of pores is significantly larger than the size of CBD regions, as expected. Note that the continuous phase size distribution of the active material phase is not considered. Instead, the size distribution of the NCM-particles will be considered in the following paragraph.

We now discuss the influence of cyclic aging on particle-based characteristics. Figure 7a) shows how the size distribution of NCM-particles is influenced by cyclic aging, where the difference between both C-rates is more pronounced for lower SOH-values. Interestingly, there are some aging scenarios for which the particle size distributions is slighted shifted towards smaller particles. On the other hand, there are

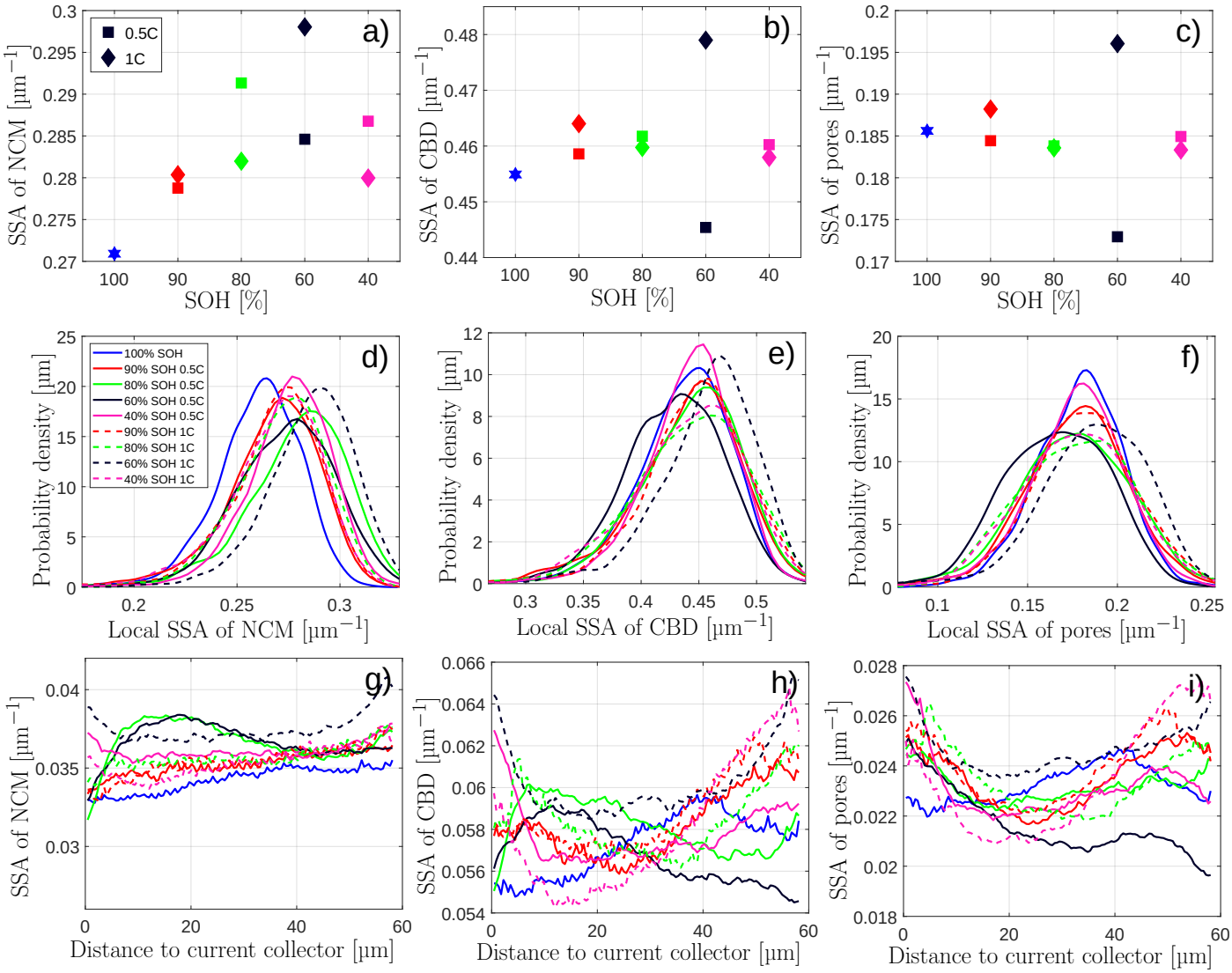


Figure 4: Specific surface area of active material (a), CBD (b) and pore space (c). Middle row: Probability density of local specific surface area of active material (d), CBD (e) and pore space (f). Bottom row: Specific surface area of active material (g), CBD (h) and pore space (i) as a function of the distance to the separator.

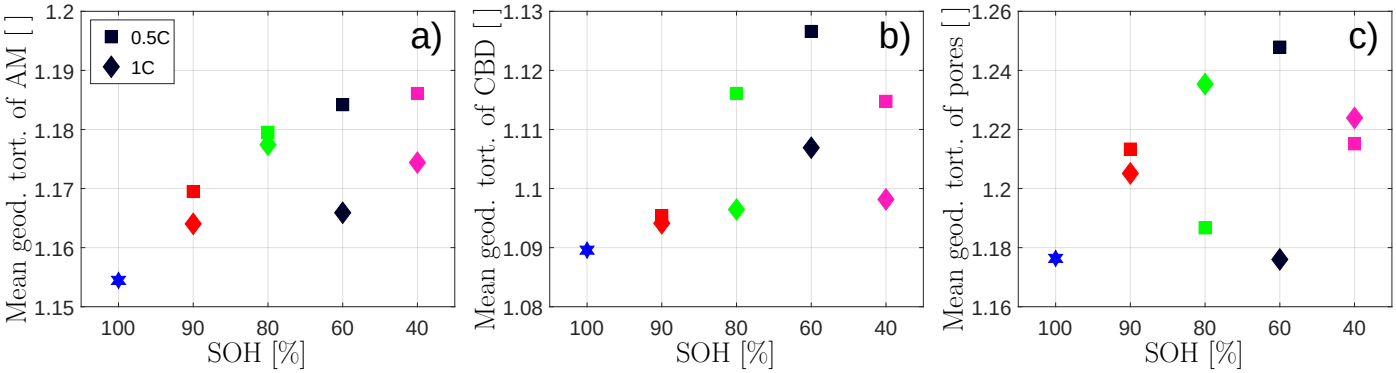


Figure 5: Mean geodesic tortuosity of active material (a), CBD (b) and pore space (c).

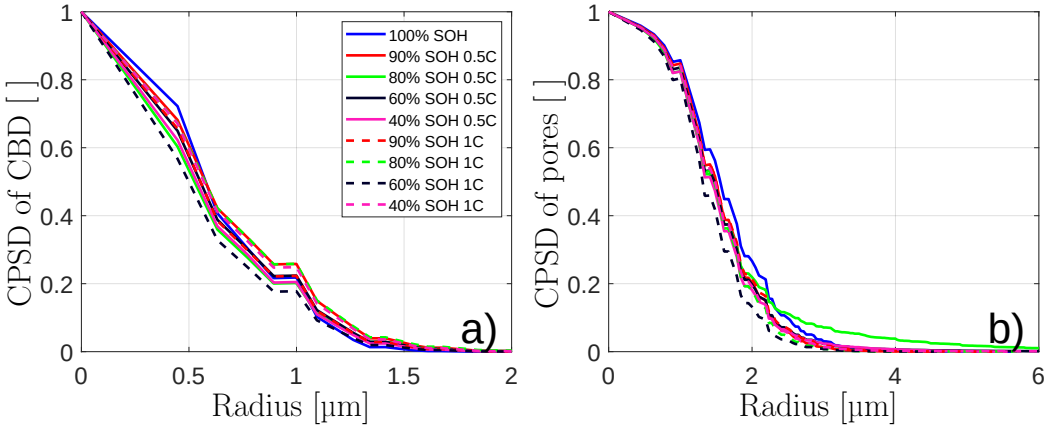


Figure 6: Normalized continuous phase size distribution of CBD (a) and pore space (b).

samples with larger particles compared to the pristine sample. In addition, Figure 7b) reveals that the sphericity distribution is clearly shifted to the left due to cyclic aging, which might be partially caused by particle cracking. However, it is likely that the NCM-particles are also mechanically deformed since at least some cathode samples do not show an increased number of small particles, which should be observed in case of particle cracking. Figure 7c) shows the distribution of the coordination number, which only depends on the C-rate for a SOH of 80% and below. Furthermore, most samples show a shift of the distribution to the right, which corresponds to a slightly improved connectivity of the system of active particles. In addition, there is a certain small fraction of NCM-particles, which are isolated from the remaining particles, for each considered cathode sample.

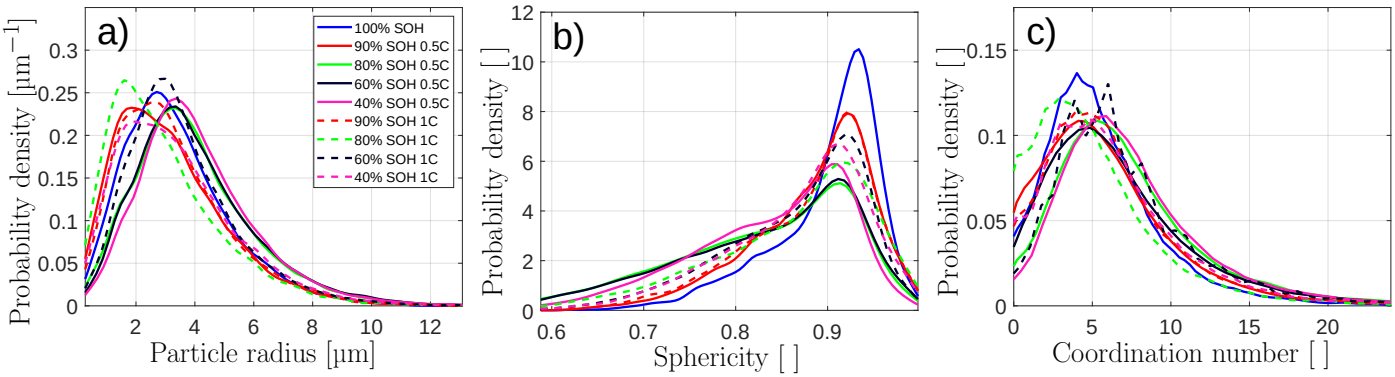


Figure 7: Probability density of size (a), sphericity (b) and coordination number (c) of active material particles. Note that for the sake of clarity, a kernel density estimation is used for the coordination number, even though this is a discrete quantity.

### *5.2. Electrochemical measurements*

The cells showed average capacities of about 40.2 mA h at 0.1C and retaining 40.01 mA h at 0.5C, and 36.45 mA h at 1C in the initial characterization. The capacity value for the chosen cycling rate for each cell is used as the reference value for the SOH instead of doing slower cycles as check-up. This is done primarily because of two reasons: First, check-up cycles need a lot of time. Depending on the chosen C-rate, the cyclic aging process including the performed electrochemical measurements already took up

to about two years. Secondly, the slower cycles have a significant influence on the aging behavior [73], which is not desired for in this study.

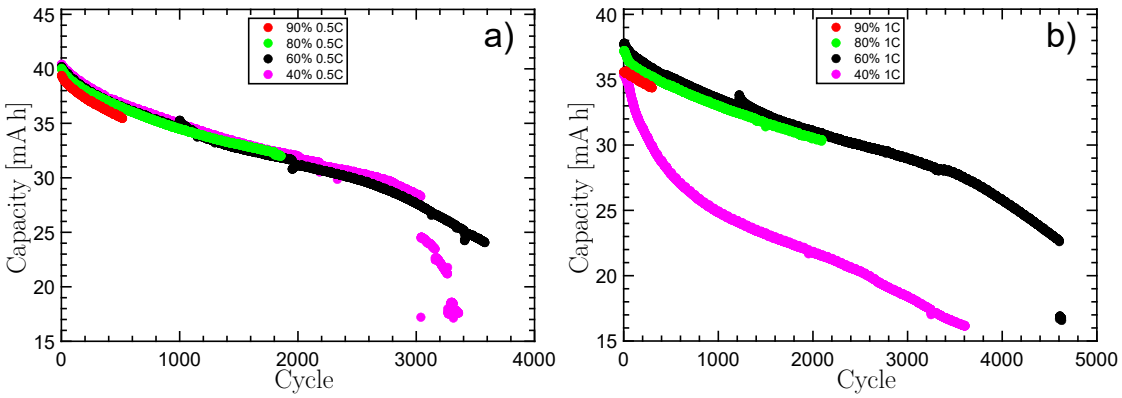


Figure 8: Discharge capacity in dependence on the cycle number for 0.5C (a) and 1C (b).

Figure 8a) shows the discharge capacity as a function of the cycle number for the cells aged at 0.5C, while Figure 8b) corresponds to a C-rate of 1C. The cells 60% 0.5C and 40% 0.5C show a steep drop in capacity at the end of their lifetime. The cell 40% 1C shows a faster aging compared to all other cells, which is a result of a slightly leaky housing or a mistake during electrolyte filling of the cell as electrolyte was detected on the outside of the housing. Unfortunately, the defect was detected after starting the experiments, so no other cell could be chosen for this long term measurement. The median of losses in capacity per cycle for each cell during the SOH steps 100% to 90%, 90% to 80%, 80% to 60% and 60% to 40% is listed in Table 2.

| cell | Capacity loss per cycle from ... to ... SOH | | | |
|---|---|---|---|---|
| | 100% - 90% | 90% - 80% | 80% - 60% | 60% - 40% |
| 0.5C 40% | 0.0098 | 0.0045 | 0.0042 | 0.0113 |
| 0.5C 60% | 0.0085 | 0.0053 | 0.0050 | - |
| 0.5C 80% | 0.0076 | 0.0043 | - | - |
| 0.5C 90% | 0.0092 | - | - | - |
| 1C 40% | 0.0213 | 0.0144 | 0.0057 | 0.0041 |
| 1C 60% | 0.0065 | 0.0049 | 0.0052 | - |
| 1C 80% | 0.0053 | 0.0031 | - | - |
| 1C 90% | 0.0067 | - | - | - |

Table 2: Capacity loss per cycle in mA h for the aged cells.

Not considering the cell 40% 1C, the cells aged at 0.5C show a faster capacity fade during the first 10% of aging compared to the 1C-cells. The next 10% SOH-change show similar rates, while the last two sections indicate that the 1C-cells are aging faster, as expected. The results of the first 20% can be explained by the increased amount of charge, which is cycled through the cells for the 0.5C rate. This leads to a greater expansion and contraction of the electrodes and, therefore, a faster aging. Higher temperatures and concentration gradients caused by a higher C-rate seem to play a secondary role in

the first 20% of SOH-reduction. Nevertheless, these effects could play a bigger role in the later part of cyclic aging.

Figure 9 shows the normalized resistances of R0, R2 and R3 for each cell in dependence of its SOH. The values are normalized to the resistances from the ECM fitted to the first EIS measurement of the corresponding cell. An increase of the internal resistance R0 can be observed for all cells that were cycled with 0.5C in the first 20% SOH loss, except for sample 0.5C 40%. The value of R0 first rises during the first 10% SOH-loss and drops over the aging process to about the original value from the first ECM fit at 40% SOH. With regard to the 1C measurements, the value of R0 is also increasing during aging except for the 90% SOH cell, which shows a slight decline of about 20%. Generally, the internal resistance of all cells never rises over 2.5 times the corresponding initial value, therefore never reaching three times the initial resistance criterion for end of life (EOL), which is frequently used in the literature [74, 75]. Examples for the EIS measurements on which these results are based can be found in the supporting information.

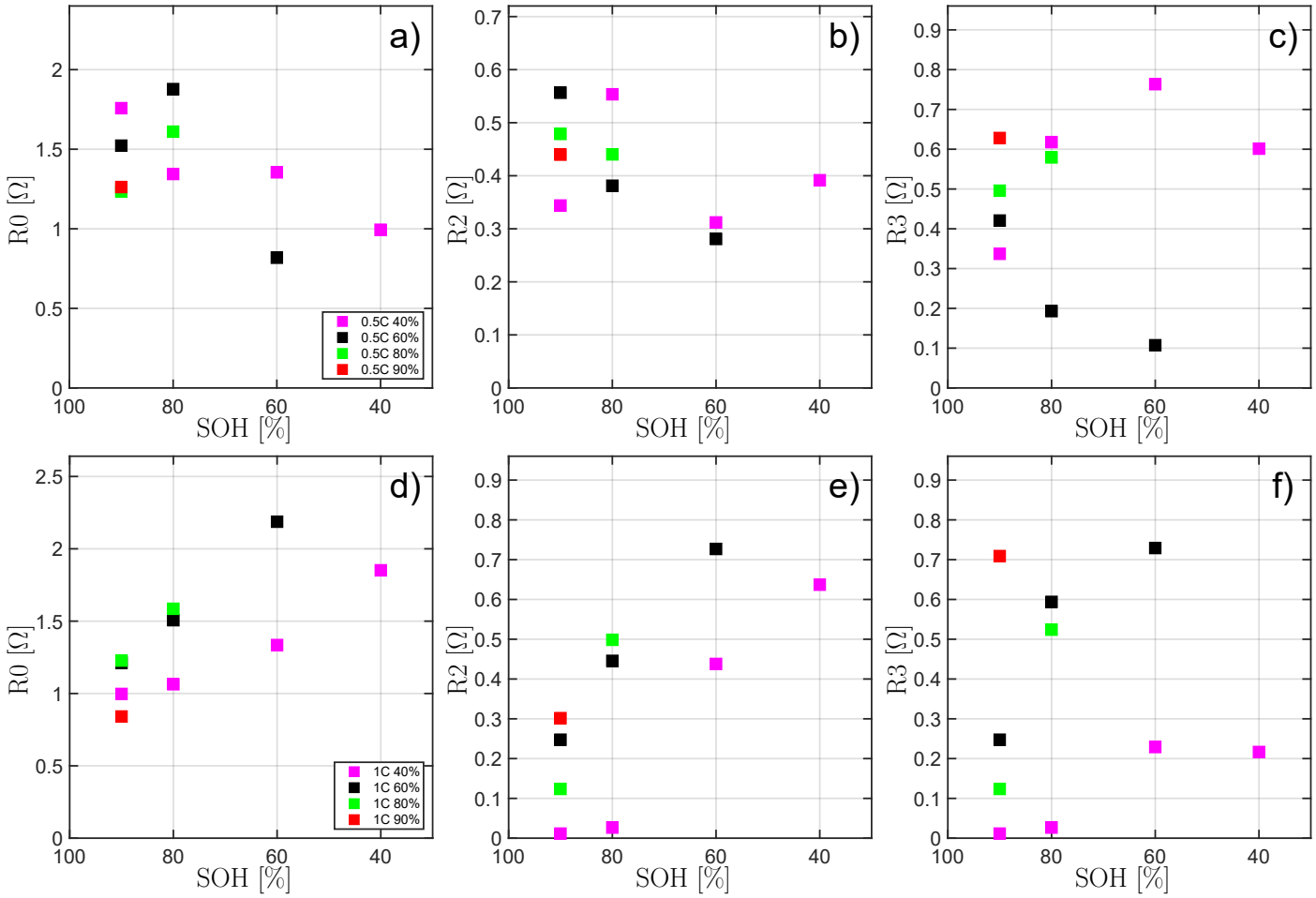


Figure 9: Development of the resistors R0, R2 and R3 in the ECM (from left to right) during aging with 0.5C (top row) and 1C (bottom row). The values are normalized to resistances from the ECM fitted to the first EIS measurement of the corresponding cell.

The curves corresponding to R2 display a quite complex behavior for the cells aged at 0.5C. The fits for

the cells corresponding to a SOH of 90% and 80% show a decreasing value, while the 60% cell shows an about 1.4 times higher value at 90% SOH and values smaller than the initial one for 80% and 60% SOH. The cell aged to 40% SOH shows normalized R2s between 1.9 and 3.5, rising from 90% to 80%, decreasing to a minimum at 60% and finishing at about 2.4 at 40% SOH. The values for R2 for the 1C measurements show a clear increasing trend during aging. They rise up by a factor of about 60 of the initial value (40% SOH), which is more than tenfold of the factor for the 0.5C aging series. The R3 parameter for the 0.5C aging series displays a lowering of the resistance for the 60% and 90% cells, while the parameter increases for the other two cells. A decrease is shown from 60% to 40% SOH for the 40% cell. The values for R3 for the 1C series show a similar behavior as the R2 values for the same series. For all values an increase in resistance is detected and only the 60% to 40% SOH step shows a slight decrease. To summarize the results shown in Figure 9, it can be stated that the 1C series shows a much clearer picture of increasing resistances, while the behavior of the cells aged at 0.5C is much more complicated. Also the increase of the resistances R2 and R3 in the 1C series is about 10 times higher than in the 0.5C series.

Generally, the volume fraction of the active material is increasing during aging, see Figure 3. At the same time, the value of R3 is rising for the 1C aging series. As can be seen in Figure 4, the SSA of the active material is rising too. This can be explained with the decreasing amount of lithium, which is extracted during discharge, due to the higher volume of a more lithiated NCM electrode [76]. The decrease in delithiated lithium is caused by a general higher resistance in the cell in combination with a fixed voltage range with no CV phase during delithiation. This is but one aspect of the interpretation of the results. Furthermore, the mean geodesic tortuosity of the active material shown in Figure 5 together with the rising SSA suggests that particle cracking is happening in a significant amount, even though not all cracks can be detected due to the limited resolution of the image data. Note that the results cannot be explained by particle cracking alone as this would lead to a lower resistance for the electrode-electrolyte passage due to the higher surface area. This matches the observations with regard to the particle size distribution as well as the sphericity distribution in Figure 7. More precisely, the behavior of these quantities indicates that there has to be a further effect besides particle cracking since there are certain cathode samples with a shift of the particle size distribution towards larger particles. In addition, the general trend that the sphericity is decreasing during cyclic aging might be caused by a combination of particle cracking and some kind of mechanical deformation.

Considering SSA, volume fraction and tortuosity of the CBD and pore phase, it seems like the active material is generally expanding into the other two phases and is blocking paths as well as separating some areas. This might be explained with an expansion of the particles over the aging process. But it can also be interpreted as a build up of some sort of surface film, which has a similar density to the particles. If it's conductivity is low it might also explain the increase in resistance of R3. To show a similar signal during the CT scan the film must be of a similar atomic number and/or structure. This leads to the conclusion, that it is one of three possible in the cell present materials: First, it could be a copper derivative from the current collector of the anode. Second, an additive in the electrolyte, which contains similar heavy atoms as nickel, cobalt or manganese breaks down on the surface of the NCM particles. Third, the active material dissolves and is redeposited on the particle surface as another structure, which is less conductive than the original material. Since it has been shown in [77] that these redepositions have a great influence on layered nickel-based cathode materials, the third possibility seems to be most likely. Nevertheless, this cannot be proved in this study and there are further possibilities, which might explain this behavior. This underlines the complex nature of aging mechanisms and forms the basis for future research.

## 6. Conclusion

In the present paper, the influence of cyclic aging on the 3D microstructure of cathodes as well as the electrochemical properties of lithium-ion battery cells is investigated. To the best of our knowledge, this is the most extensive data set of cyclically aged lithium-ion cells including electrochemical data as well as 3D structures. More precisely, synchrotron tomography is used to capture the 3D microstructure of cyclically aged cathodes, where two different C-rates (0.5C and 1C) and five different values for the state of health (100%, 90%, 80%, 60% and 40%) are considered. The resulting 3D image data is segmented by a $k$-means clustering approach into three phases, namely active material, carbon-binder domain and pore space. In addition, a particle-based segmentation of the system of active material particles is carried out by a combination of morphological reconstruction and the watershed algorithm. The processed image data allows for a comprehensive microstructural analysis, which among others shows that even though the changes with regard to the volume fraction of each phase are small, there are more pronounced changes when considering the volume fraction as a function of the distance to the current collector. This emphasizes the importance of 3D measurements as well as local descriptors of 3D microstructure in order to accurately capture the morphology of electrodes since certain important structural effects can not be detected by using 2D image data or globally computed microstructure properties. Besides the morphological point of view, cyclic aging is quantitatively investigated by means of electrochemical impedance spectroscopy, where the resulting data is fitted by an equivalent circuit model. Among others, it has been shown that a C-rate of 0.5 leads to a complex aging behavior, whereas cyclic aging at 1C leads to a clearer picture of increased resistances which are up to ten times higher compared to the 0.5C cells. A correlation to structural data shows another factor than particle cracking, which is more dominant than particle cracking.

## Acknowledgment

This work was financially supported by the "Bundesministerium für Bildung und Forschung" (BMBF) through the research grants No. 05M18VUA and 05M18VSA. We are grateful to VARTA Microbattery GmbH for providing the cells. Furthermore, we thank Marten Ademmer and Lukas Petrich for their valuable feedback, which helped us to further improve the quality of this manuscript.

## References

[1] B. Scrosati, K. M. Abraham, W. van Schalkwijk, and J. Hassoun, eds., Lithium Batteries: Advanced Technologies and Applications. The Electrochemical Society Series, Hoboken: J. Wiley & Sons, 2013.

[2] R. Korthauer, Lithium-Ion Batteries: Basics and Applications. Berlin: Springer, 2018.

[3] C. Julien, A. Mauger, A. Vijh, and K. Zaghib, Lithium Batteries: Science and Technology. Cham: Springer International Publishing, 2016.

[4] J. B. Goodenough and K.-S. Park, "The Li-ion rechargeable battery: A perspective," Journal of the American Chemical Society, vol. 135, no. 4, 1167–1176, 2013.

[5] J. Newman and K. Thomas-Alyea, Electrochemical Systems. The ECS Series of Texts and Monographs, Hoboken: J. Wiley & Sons, 3rd ed., 2004.

[6] B. Huang, G. Li, Z. Pan, X. Su, and L. An, "Enhancing high-voltage performance of $LiNi_{0.5}Co_{0.2}Mn_{0.3}O_2$ cathode material via surface modification with lithium-conductive $Li_3Fe_2(PO_4)_3$," Journal of Alloys and Compounds, vol. 773, 519–526, 2019.

[7] F. Zhang, T. Geng, F. Peng, D. Zhao, N. Zhang, H. Zhang, and S. Li, "New insights for the abuse tolerance behavior of $LiMn_2O_4$ under high cut-off potential conditions," ChemElectroChem, vol. 6, no. 3, 731–740, 2019.

[8] G. Li, B. Huang, Z. Pan, X. Su, Z. Shao, and L. An, "Advances in three-dimensional graphene-based materials: configurations, preparation and application in secondary metal (Li,Na,K,Mg,Al)-ion batteries," Energy Environmental Science, vol. 12, 2030–2053, 2019.

[9] A. Barré, B. Deguilhem, S. Grolleau, M. Gérard, F. Suard, and D. Riu, "A review on lithium-ion battery ageing mechanisms and estimations for automotive applications," Journal of Power Sources, vol. 241, 680–689, 2013.

[10] M. Broussely, P. Biensan, F. Bonhomme, P. Blanchard, S. Herreyre, K. Nechev, and R. Staniewicz, "Main aging mechanisms in li ion batteries," Journal of Power Sources, vol. 146, no. 1, 90–96, 2005.

[11] F. Single, B. Horstmann, and A. Latz, "Theory of impedance spectroscopy for lithium batteries," The Journal of Physical Chemistry C, vol. 123, no. 45, 27327–27343, 2019.

[12] T. Heil, Ersatzschaltbild-basierte Modellierung der Diffusion und des Ladungsdurchtritts in Lithium-Ionen-Zellen. PhD thesis, Technische Universität München, 2020.

[13] S. Cho, C.-F. Chen, and P. P. Mukherjee, "Influence of microstructure on impedance response in intercalation electrodes," Journal of The Electrochemical Society, vol. 162, no. 7, A1202–A1214, 2015.

[14] A. H. Wiedemann, G. M. Goldin, S. A. Barnett, H. Zhu, and R. J. Kee, "Effects of three-dimensional cathode microstructure on the performance of lithium-ion battery cathodes," Electrochemica Acta, vol. 88, 580–588, 2013.

[15] W. Li and J. C. Currie, "Morphology effects on the electrochemical performance of $LiNi_{1-x}Co_xO_2$," Journal of The Electrochemical Society, vol. 144, no. 8, 2773–2779, 1997.

[16] Y. Shin and A. Manthiram, "Influence of microstructure on the electrochemical performance of $LiMn_{2-y-z}Li_yNi_zO_4$ spinel cathodes in rechargeable lithium batteries," Journal of Power Sources, vol. 126, no. 1, 169–174, 2004.

[17] V. Yufit, P. Shearing, P. D. Lee, M. Wu, and N. P. Brandon, "Investigation of lithium-ion polymer battery cell failure using X-ray computed tomography," Electrochemistry Communications, vol. 13, no. 6, 608–610, 2011.

[18] A. S. Mussa, A. Liivat, F. Marzano, M. Klett, B. Philippe, C. Tengstedt, G. Lindbergh, K. Edström, R. W. Lindström, and P. Svens, "Fast-charging effects on ageing for energy-optimized automotive $LiNi_{1/3}Mn_{1/3}Co_{1/3}O_2$/graphite prismatic lithium-ion cells," Journal of Power Sources, vol. 422, 175–184, 2019.

[19] E. M. Börger, E. Jochler, J. Kaufmann, R. Ramme, A. Grimm, S. Nowak, F. M. Schappacher, U. Rodehorst, A.-C. Voigt, S. Passerini, M. Winter, and A. Börger, "Aging of ceramic coated graphitic negative and NCA positive electrodes in commercial lithium-ion battery cells – an ex-situ study of different states of health for identification and quantification of aging influencing parameters," Journal of Energy Storage, vol. 13, 304–312, 2017.

[20] B. Prifling, A. Ridder, A. Hilger, M. Osenberg, I. Manke, K. P. Birke, and V. Schmidt, "Analysis of structural and functional aging of electrodes in lithium-ion batteries during rapid charge and discharge rates using synchrotron tomography," Journal of Power Sources, vol. 443, 227259, 2019.

[21] J. Warner, Lithium-Ion Battery Chemistries: A Primer. Amsterdam: Elsevier Science, 2019.

[22] F. Huttner, A. Diener, T. Heckmann, J. C. Eser, T. Abali, J. K. Mayer, P. Scharfer, W. Schabel, and A. Kwade, "Increased moisture uptake of NCM622 cathodes after calendering due to particle breakage," Journal of The Electrochemical Society, vol. 168, no. 9, 090539, 2021.

[23] A. J. Smith, J. C. Burns, X. Zhao, D. Xiong, and J. R. Dahn, "A high precision coulometry study of the SEI growth in Li/Graphite cells," Journal of The Electrochemical Society, vol. 158, no. 5, A447, 2011.

[24] I. Khokhriakov, L. Lottermoser, R. Gehrke, T. Kracht, E. Wintersberger, A. Kopmann, M. Vogelgesang, and F. Beckmann, "Integrated control system environment for high-throughput tomography," in Developments in X-Ray Tomography IX (S. R. Stock, ed.), vol. 9212, 307–317, International Society for Optics and Photonics, SPIE, 2014.

[25] F. Wilde, M. Ogurreck, I. Greving, J. U. Hammel, F. Beckmann, A. Hipp, L. Lottermoser, I. Khokhriakov, P. Lytaev, T. Dose, H. Burmester, M. Müller, and A. Schreyer, "Micro-CT at the imaging beamline P05 at PETRA III," AIP Conference Proceedings, vol. 1741, no. 1, 030035, 2016.

[26] W. Görner, M. Hentschel, B. Müller, H. Riesemeier, M. Krumrey, G. Ulm, W. Diete, U. Klein, and R. Frahm, "BAMline: the first hard X-ray beamline at BESSY II," Nuclear Instruments and Methods in Physics Research Section A: Accelerators, Spectrometers, Detectors and Associated Equipment, vol. 467–468, 703–706, 2001. 7th International Conference on Synchrotron Radiation Instrumentation.

[27] L. I. Rudin, S. Osher, and E. Fatemi, "Nonlinear total variation based noise removal algorithms," Physica D: Nonlinear Phenomena, vol. 60, no. 1, 259–268, 1992.

[28] B. A. Dowd, G. H. Campbell, R. B. Marr, V. V. Nagarkar, S. V. Tipnis, L. Axe, and D. P. Siddons, "Developments in synchrotron X-ray computed microtomography at the National Synchrotron Light Source," in Developments in X-Ray Tomography II (U. Bonse, ed.), vol. 3772, 224–236, International Society for Optics and Photonics, SPIE, 1999.

[29] R. C. Gonzalez and R. E. Woods, Digital Image Processing. New Jersey: Prentice Hall, 3rd ed., 2008.

[30] A. Buades, B. Coll, and J.-M. Morel, "A non-local algorithm for image denoising," in Proceedings of the IEEE Computer Society Conference on Computer Vision and Pattern Recognition, vol. 2, (San Diego), pp. 60–65, IEEE Computer Society, 2005.

[31] P. Coupé, P. Yger, S. Prima, P. Hellier, C. Kervrann, and C. Barillot, "An optimized blockwise nonlocal means denoising filter for 3-D magnetic resonance images," IEEE Transactions on Medical Imaging, vol. 27, no. 4, 425–441, 2008.

[32] E. Machado Charry, M. Neumann, J. Lahti, R. Schennach, V. Schmidt, and K. Zojer, "Pore space extraction and characterization of sack paper using μ-CT," Journal of Microscopy, vol. 272, no. 1, 35–46, 2018.

[33] L. Zielke, T. Hutzenlaub, D. R. Wheeler, C.-W. Chao, I. Manke, A. Hilger, N. Paust, R. Zengerle, and S. Thiele, "Three-phase multiscale modeling of a $LiCoO_2$ cathode: Combining the advantages of FIB-SEM imaging and X-ray tomography," Advanced Energy Materials, vol. 5, no. 5, 1401612, 2015.

[34] S. Vierrath, L. Zielke, R. Moroni, A. Mondon, D. R. Wheeler, R. Zengerle, and S. Thiele, "Morphology of nanoporous carbon-binder domains in Li-ion batteries–a FIB-SEM study," Electrochemistry Communications, vol. 60, 176–179, 2015.

[35] M. J. D. Powell, "The BOBYQA algorithm for bound constrained optimization without derivatives," Cambridge NA Report NA2009/06, 26–46, 2009. University of Cambridge, Cambridge.

[36] S. Beucher and F. Meyer, "The morphological approach to segmentation: the watershed transformation," in Mathematical Morphology in Image Processing (E. R. Dougherty, ed.), pp. 433–481, New York: Marcel Dekker Inc., 1993.

[37] R. Beare and G. Lehmann, "The watershed transform in ITK – discussion and new developments," The Insight Journal, vol. 6, 2006.

[38] J. B. T. M. Roerdink and A. Meijster, "The watershed transform: Definitions, algorithms and parallelization strategies," Fundamenta Informaticae, vol. 41, 187–228, 2000.

[39] A. Spettl, R. Wimmer, T. Werz, M. Heinze, S. Odenbach, C. Krill III, and V. Schmidt, "Stochastic 3D modeling of Ostwald ripening at ultra-high volume fractions of the coarsening phase," Modelling and Simulation in Materials Science and Engineering, vol. 23, no. 6, 065001, 2015.

[40] K. Kuchler, W. Westhoff, J. Feinauer, T. Mitsch, I. Manke, and V. Schmidt, "Stochastic model for the 3D microstructure of pristine and cyclically aged cathodes in Li-ion batteries," Modelling and Simulation in Materials Science and Engineering, vol. 26, no. 3, 035005, 2018.

[41] K. Kuchler, B. Prifling, D. Schmidt, H. Markötter, I. Manke, T. Bernthaler, V. Knoblauch, and V. Schmidt, "Analysis of the 3D microstructure of experimental cathode films for lithium-ion batteries under increasing compaction," Journal of Microscopy, vol. 272, no. 2, 96–110, 2018.

[42] J. Zheng and R. D. Hryciw, "Segmentation of contacting soil particles in images by modified watershed analysis," Computers and Geotechnics, vol. 73, 142–152, 2016.

[43] J. C. Russ, The Image Processing Handbook. Boca Raton: CRC Press, $5^{th}$ ed., 2007.

[44] W. Burger and M. Burge, Digital Image Processing: An Algorithmic Introduction Using Java. London: Springer, $2^{nd}$ ed., 2016.

[45] P. Soille, Morphological Image Analysis: Principles and Applications. New York: Springer, 2nd ed., 2003.

[46] J. Serra, Image Analysis and Mathematical Morphology. London: Academic Press, 1982.

[47] L. Najman and H. Talbot, Mathematical Morphology: From Theory to Applications. Hoboken: J. Wiley & Sons, 2010.

[48] L. Vincent, "Morphological grayscale reconstruction in image analysis: applications and efficient algorithms," IEEE Transactions on Image Processing, vol. 2, no. 2, 176–201, 1993.

[49] S. N. Chiu, D. Stoyan, W. S. Kendall, and J. Mecke, Stochastic Geometry and its Applications. Chichester: J. Wiley & Sons, 3rd ed., 2013.

[50] K. Schladitz, J. Ohser, and W. Nagel, "Measuring intrinsic volumes in digital 3D images," in 13th International Conference Discrete Geometry for Computer Imagery (A. Kuba, L. Nyúl, and K. Palágyi, eds.), pp. 247–258, Springer, 2007.

[51] M. B. Clennell, "Tortuosity: a guide through the maze," Geological Society, London, Special Publications, vol. 122, no. 1, 299–344, 1997.

[52] B. Tjaden, D. J. L. Brett, and P. R. Shearing, "Tortuosity in electrochemical devices: a review of calculation approaches," International Materials Reviews, vol. 63, no. 2, 47–67, 2018.

[53] B. Ghanbarian, A. G. Hunt, R. P. Ewing, and M. Sahimi, "Tortuosity in porous media: a critical review," Soil Science Society of America Journal, vol. 77, no. 5, 1461–1477, 2013.

[54] L. Holzer, B. Iwanschitz, T. Hocker, L. Keller, O. M. Pecho, G. Sartoris, P. Gasser, and B. Muench, "Redox cycling of Ni–YSZ anodes for solid oxide fuel cells: Influence of tortuosity, constriction and percolation factors on the effective transport properties," Journal of Power Sources, vol. 242, 179–194, 2013.

[55] O. Stenzel, O. M. Pecho, L. Holzer, M. Neumann, and V. Schmidt, "Predicting effective conductivities based on geometric microstructure characteristics," AIChE Journal, vol. 62, no. 5, 1834–1843, 2016.

[56] B. Prifling, M. Röding, P. Townsend, M. Neumann, and V. Schmidt, "Large-scale statistical learning for mass transport prediction in porous materials using 90,000 artificially generated microstructures," Frontiers in Materials, vol. 8, 786502, 2021.

[57] D. Jungnickel, Graphs, Networks and Algorithms. Berlin: Springer, 3rd ed., 2008.

[58] M. Neumann, C. Hirsch, J. Staněk, V. Beneš, and V. Schmidt, "Estimation of geodesic tortuosity and constrictivity in stationary random closed sets," Scandinavian Journal of Statistics, vol. 46, no. 3, 848–884, 2019.

[59] G. Matheron, Random Sets and Integral Geometry. New York: J. Wiley & Sons, 1975.

[60] H. Wadell, "Volume, shape and roundness of quart particles," The Journal of Geology, vol. 43, 250–280, 1935.

[61] W. A. Paxton, Z. Zhong, and T. Tsakalakos, "Tracking inhomogeneity in high-capacity lithium iron phosphate batteries," Journal of Power Sources, vol. 275, 429–434, 2015.

[62] S. J. Harris and P. Lu, "Effects of inhomogeneities – nanoscale to mesoscale – on the durability of Li-ion batteries," The Journal of Physical Chemistry C, vol. 117, no. 13, 6481–6492, 2013.

[63] M. M. Forouzan, B. A. Mazzeo, and D. R. Wheeler, "Modeling the effects of electrode microstructural heterogeneities on Li-ion battery performance and lifetime," Journal of The Electrochemical Society, vol. 165, no. 10, A2127–A2144, 2018.

[64] L. Cai, K. An, Z. Feng, C. Liang, and S. J. Harris, "In-situ observation of inhomogeneous degradation in large format Li-ion cells by neutron diffraction," Journal of Power Sources, vol. 236, 163–168, 2013.

[65] J. Cannarella and C. B. Arnold, "The effects of defects on localized plating in lithium-ion batteries," Journal of The Electrochemical Society, vol. 162, no. 7, A1365–A1373, 2015.

[66] J. E. Vogel, M. M. Forouzan, E. E. Hardy, S. T. Crawford, D. R. Wheeler, and B. A. Mazzeo, "Electrode microstructure controls localized electronic impedance in Li-ion batteries," Electrochimica Acta, vol. 297, 820–825, 2019.

[67] D. Kehrwald, P. R. Shearing, N. P. Brandon, P. K. Sinha, and S. J. Harris, "Local tortuosity inhomogeneities in a lithium battery composite electrode," Journal of The Electrochemical Society, vol. 158, no. 12, A1393, 2011.

[68] B. Prifling, M. Ademmer, F. Single, O. Benevolenski, A. Hilger, M. Osenberg, I. Manke, and V. Schmidt, "Stochastic 3D microstructure modeling of anodes in lithium-ion batteries with a particular focus on local heterogeneity," Computational Materials Science, vol. 192, 110354, 2021.

[69] W. J. Hagiwara H., Suszynski and L. F. Francis, "A Raman spectroscopic method to find binder distribution in electrodes during drying," Journal of Coatings Technology and Research, vol. 11, 11–17, 2014.

[70] F. Font, B. Protas, G. Richardson, and J. Foster, "Binder migration during drying of lithium-ion battery electrodes: Modelling and comparison to experiment," Journal of Power Sources, vol. 393, 177–185, 2018.

[71] L. S. Kremer, A. Hoffmann, T. Danner, S. Hein, B. Prifling, D. Westhoff, C. Dreer, A. Latz, V. Schmidt, and M. Wohlfahrt-Mehrens, "Manufacturing process for improved ultra-thick cathodes in high-energy lithium-ion batteries," Energy Technology, vol. 8, no. 2, 1900167, 2020.

[72] S. Lim, K. H. Ahn, and M. Yamamura, "Latex migration in battery slurries during drying," Langmuir, vol. 29, no. 26, 8233–8244, 2013.

[73] R. Mingant, J. Bernard, and V. Sauvant-Moynot, "Novel state-of-health diagnostic method for li-ion battery in service," Applied Energy, vol. 183, 390–398, 2016.

[74] J. Groenewald, T. Grandjean, and J. Marco, "Accelerated energy capacity measurement of lithium-ion cells to support future circular economy strategies for electric vehicles," Renewable and Sustainable Energy Reviews, vol. 69, 98–111, 2017.

[75] E. Wood, M. Alexander, and T. H. Bradley, "Investigation of battery end-of-life conditions for plug-in hybrid electric vehicles," Journal of Power Sources, vol. 196, no. 11, 5147–5154, 2011.

[76] T. Bartsch, A.-Y. Kim, F. Strauss, L. de Biasi, J. H. Teo, J. Janek, P. Hartmann, and T. Brezesinski, "Indirect state-of-charge determination of all-solid-state battery cells by X-ray diffraction," Chemical Communications, vol. 55, 11223–11226, 2019.

[77] M. Evertz, F. Horsthemke, J. Kasnatscheew, M. Börner, M. Winter, and S. Nowak, "Unraveling transition metal dissolution of $Li_{1.04}Ni_{1/3}Co_{1/3}Mn_{1/3}O_2$ (NCM 111) in lithium ion full cells by using the total reflection X-ray fluorescence technique," Journal of Power Sources, vol. 329, 364–371, 2016.

## Appendix

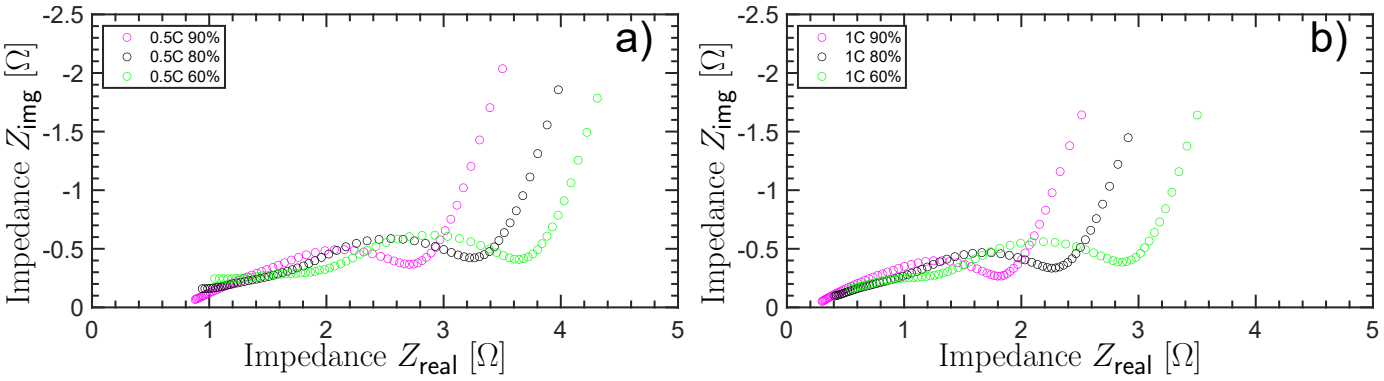


Figure A1: Nyquist plots corresponding to the C-rates of 0.5C (a) and 1C (b) for both 60% SOH cells, where for exactly these two cells the spectra for the SOH values of 90%, 80% and 60% are shown.